Electronic Supplementary Material (ESI) for Journal of Materials Chemistry A.

Supporting Information

Synergistic boron-dopants and boron-induce oxygen vacancies in MnO_2 nanosheets to promote electrocatalytic nitrogen reduction

Ke Chu*, Ya-ping Liu, Yong-hua Cheng, Qing-qing Li

School of Materials Science and Engineering, Lanzhou Jiaotong University, Lanzhou 730070, China

*Corresponding author. E-mail address: chukelut@163.com (K. Chu)

Experimental

Synthesis of B-MnO$_2$

All the chemicals were used as received without further purification. Typically, a piece of as-obtained CC (1 cm × 4 cm) was ultrasonically treated in concentrated HCl for 1 h, and cleaned with ethanol and distilled water several times. Then, 2 mM of $KMnO_4$ and 0.03 mM of $NH_4HB_4O_7 \cdot 3H_2O$ were diluted into 40 mL of distilled water. The mixed solution was transferred into a Teflon-lined stainless-steel autoclave, following by immersing the pretreated CC in the solution. The autoclave was sealed and kept at 180 °C for 16 h in an oven. After cooling to room temperature, the obtained B-MnO_2/CC was washed with deionized water and ethanol several times, and dried at 60 ^{o}C overnight. For comparison, the pristine MnO_2/CC was prepared by the same procedure without addition of $NH_4HB_4O_7 \cdot 3H_2O$.

Electrochemical measurements

Electrochemical measurements were tested on a CHI-660E electrochemical workstation. The prepared CC sample was directly used as a working electrode. The graphite rod and Ag/AgCl were used as reference and counter electrodes, respectively. All potentials were referenced to the reversible hydrogen electrode (RHE). The RHE calibration was experimentally conducted in the high-purity hydrogen saturated 0.5 M $LiClO_4$ electrolyte by cyclic voltammeters curves, with using graphite rod and Pt wire as counter and working electrodes, respectively (Fig. S2). The NRR tests were conducted in an H-type two-compartment electrochemical cell separated by a Nafion 211 membrane. An absorber was set at the end of cell to avoid the loss of produced NH_3 by N_2 flow. The Nafion membrane was pretreated by boiling it in 5% H_2O_2 solution for 1 h, 0.5 M H_2SO_4 for 1 h and deionized water for 1 h in turn. Prior to each electrolysis, the cathodic compartment was purged with Ar for 30 min. During each electrolysis, ultra-high-purity N_2 gas (99.999%) was continuously purged into the cathodic chamber at a flow rate of 20 mL min^{-1}. After each NRR electrolysis, the solution in absorber was poured back into the cathodic compartment for the NH_3 detection. The produced NH_3 and possible N_2H_4 were quantitatively determined by the indophenol blue method[1], and approach of Watt and Chrisp[2], respectively.

Determination of N_2H_4

Typically, 5 mL of electrolyte was removed from the electrochemical reaction vessel. The 330 mL of color reagent containing 300 mL of ethyl alcohol, 5.99 g of $C_9H_{11}NO$ and 30 mL of HCl were prepared, and 5 mL of color reagent was added into the electrolyte. After stirring for 10 min, the UV-vis absorption spectrum was measured and the concentration-absorbance curves were calibrated by the standard N_2H_4 solution with a serious of concentrations.

Determination of NH_3

Typically, 4 mL of electrolyte was removed from the electrochemical reaction vessel. Then 50 μL of solution containing NaOH (0.75 M) and NaClO (ρ_{Cl} = ~4.5), 500 μL of solution containing 0.32 M NaOH, 0.4 M $C_7H_6O_3Na$, and 50 μL of $C_5FeN_6Na_2O$ solution (1 wt%) were respectively added into the electrolyte. After standing for 2 h, the UV-Vis absorption spectrum was measured and the concentration-absorbance curves were calibrated by the standard NH_4Cl solution with a serious of concentrations.

NH_3 yield was calculated by the following equation:

$$\mathrm{NH_3\ yield}\ (\mu\mathrm{g\ h^{-1}\ mg_{cat.}^{-1}}) = \frac{c_{\mathrm{NH_3}} \times V}{t \times m} \tag{1}$$

Faradaic efficiency was calculated by the following equation:

$$\text{Faradaic efficiency (\%)} = \frac{3 \times F \times c_{\mathrm{NH_3}} \times V}{17 \times Q} \times 100\% \tag{2}$$

where c_{NH3} (μg mL^{-1}) is the measured NH_3 concentration, V (mL) is the volume of the electrolyte, t (h) is the reduction time and m (mg) is the mass loading of the catalyst on CC. F (96500 C mol^{-1}) is the Faraday constant, Q (C) is the quantity of applied electricity.

Characterizations

Scanning electron microscopy (SEM) was performed on a JSM-6701 microscope. Transmission electron microscopy (TEM), high-resolution transmission electron microscopy (HRTEM), and high-angle annular dark field (HAADF)-scanning transmission electron microscopy (STEM) were conducted on a Tecnai G^2 F20 microscope. X-ray diffraction (XRD) pattern was performed on a Rigaku D/max 2400 diffractometer. Nitrogen adsorption/desorption isotherms were recorded on an ASAP 2020 instrument. X-ray photoelectron spectroscopy (XPS) analysis was recorded on a PHI 5702 spectrometer. Ion chromatogram measurements were conducted on a Dionex ICS-2000 ion chromatographs. ^{1}H nuclear magnetic resonance (NMR) measurements were performed on a 500 MHz Bruker superconducting-magnet NMR spectrometer. Prior to NMR measurements, $^{14}N_2$ or $^{15}N_2$ feed gas was purified by an acid trap (0.05 M H_2SO_4) to eliminate the potential NO_x and NH_3 contaminants.

Calculation details

All calculations were carried out using spin-polarized density functional theory (DFT) conducted on a Cambridge sequential total energy package (CASTEP)[3]. The generalized gradient approximation (GGA) of Perdew−Becke−Ernzerhof (PBE) is used for the exchange−correlation interactions. DFT-D scheme was adopted to account for the van der Waals interactions throughout the calculations. During structure optimization, the energy change criterion was set to 2×10^{-5} eV and 0.01 eV/Å for the energy and forces, respectively. A plane-wave basis set with an energy cutoff of 500 eV was used and the Brillouin zone was sampled in a 3×3×1 mesh. The MnO_2 (001) was modeled by a three-layered 3×3×1 supercell, and a vacuum region of 20 Å was used to separate adjacent slabs. During the calculations, all the atoms of the slab model were fully relaxed.

The computational hydrogen electrode (CHE) model was used to calculate the Gibbs free energy change (ΔG) of reaction steps:

$$\Delta G = \Delta E + \Delta ZPE - T\Delta S + \Delta G_{\mathrm{U}} + \Delta G_{\mathrm{pH}} \tag{3}$$

where ΔE is the electronic energy difference, ΔZPE is the zero point energy difference, T is the room temperature (298 K) and ΔS is the entropy change. ΔG_{U} is the contribution of electrode potential, which can be calculated by: $\Delta G_{\mathrm{U}} = -eU$, where and U is the applied potential. ΔG_{pH} is the free energy correction of pH, which can be calculated by: $\Delta G_{pH} = -k_B T \times pH \times \ln 10$, where k_B is the Boltzmann constant, and the value of pH was set to be 7 for neutral medium used in our work. The transition state of water dissociation was analyzed by a combined linear synchronous transit (LST) and quadratic synchronous transit (QST) tools.

The formation energy (E_f) of MnO_2 containing either surface B-dopant (B-MnO_2), or OV(OV-MnO_2), or both (B-OV-MnO_2) can be defined as:

$$E_f(\text{B-MnO}_2) = E(\text{B-MnO}_2) - E(\text{MnO}_2) - \mu_B + \mu_O \quad (4)$$

$$E_f(\text{MnO}_2\text{-OV}) = E(\text{MnO}_2\text{-OV}) - E(\text{MnO}_2) + \mu_O \quad (5)$$

$$E_f(\text{B-OV-MnO}_2) = E(\text{B-OV-MnO}_2) - E(\text{MnO}_2) - \mu_B + \mu_{Mn(O)} + \mu_O \quad (6)$$

where E is the total energies of corresponding structures, μ is the chemical potential of corresponding atoms.

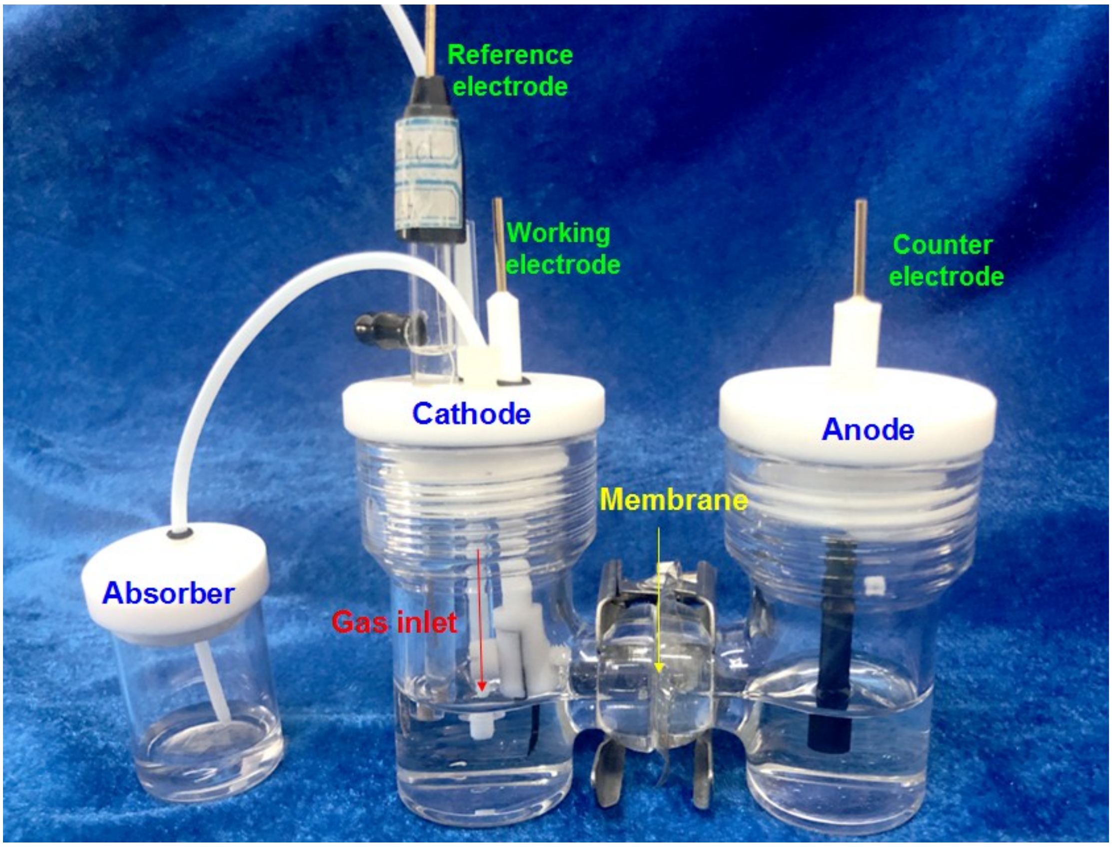

Fig. S1. Photograph of H-type electrochemical setup.

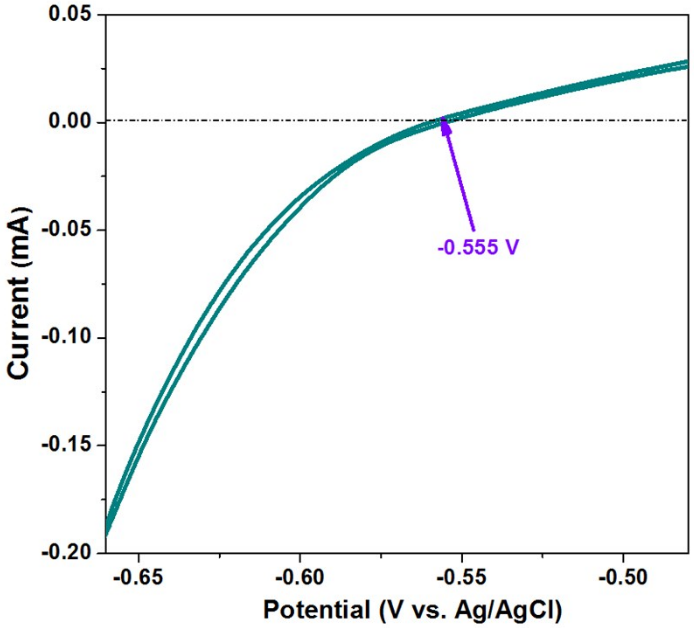

Fig. S2. The RHE calibration in 0.5 M $LiClO_4$ electrolyte.

The RHE calibration was conducted in the high-purity hydrogen saturated 0.5 M $LiClO_4$ electrolyte. The graphite rod and Pt wire were used as the counter and working electrodes, respectively. The cyclic voltammetry curves were performed at a scan rate of 1 mV s^{-1}. The RHE calibration potential for the hydrogen oxidation/evolution reactions is the average value of the two potentials at which the current crosses zero. It is shown in Fig. S2 that the *E*(RHE) is larger than *E*(Ag/AgCl) by 0.555 V. Therefore, we have *E*(RHE) = *E*(Ag/AgCl) +0.555.

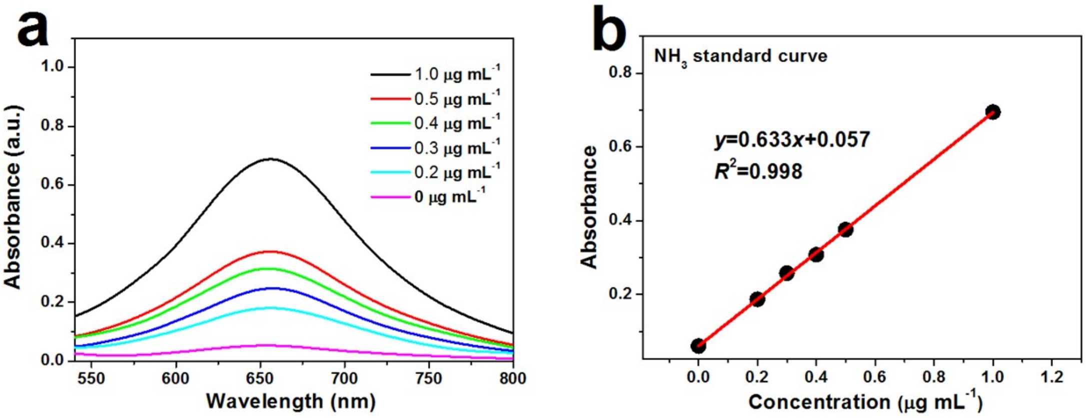

Fig. S3. (a) UV-Vis absorption spectra of indophenol assays with NH_4Cl after incubated for 2 h at ambient conditions. (b) Calibration curve used for calculation of NH_3 concentrations.

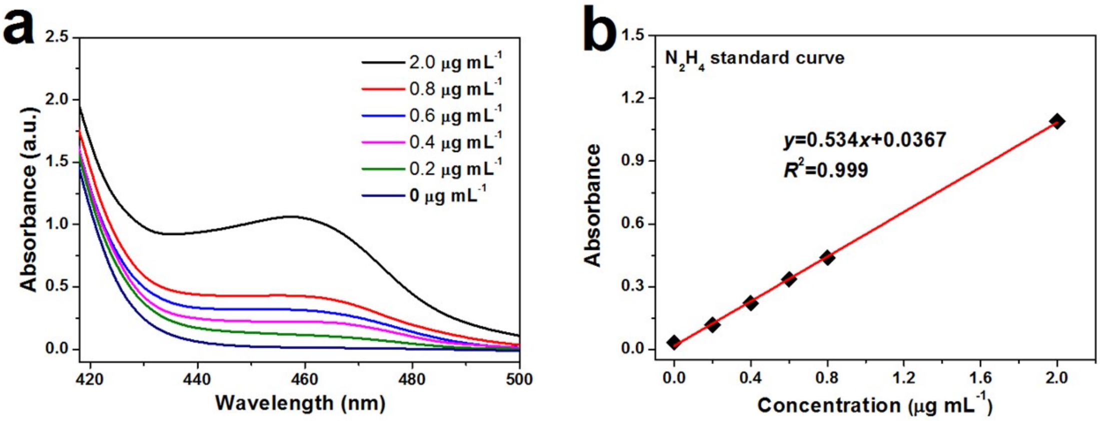

Fig. S4. (a) UV-Vis absorption spectra of N_2H_4 assays after incubated for 20 min at ambient conditions. (b) Calibration curve used for calculation of N_2H_4 concentrations.

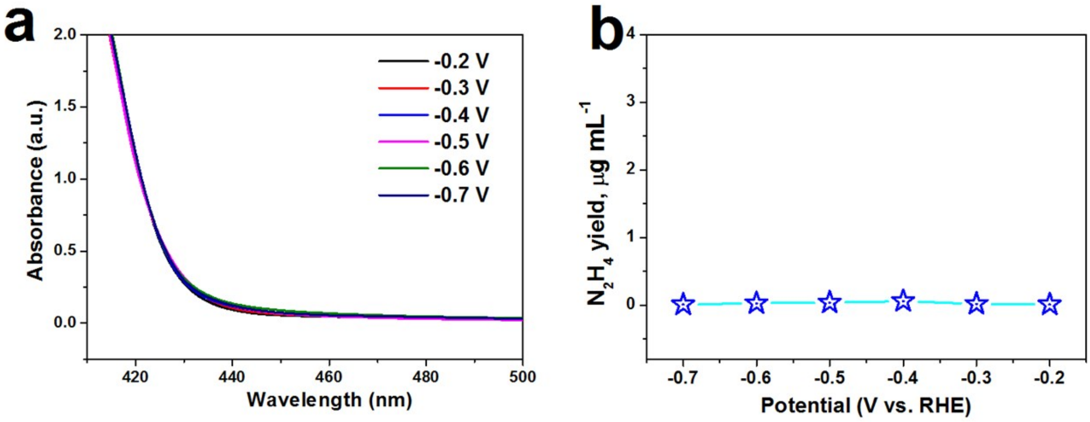

Fig. S5. (a) UV-Vis spectra of the electrolytes (stained with the chemical indicator based on the method of Watt and Chrisp) after 2 h electrocatalysis on B-MnO_2/CC at various potentials, and (b) corresponding N_2H_4 concentrations in the electrolytes.

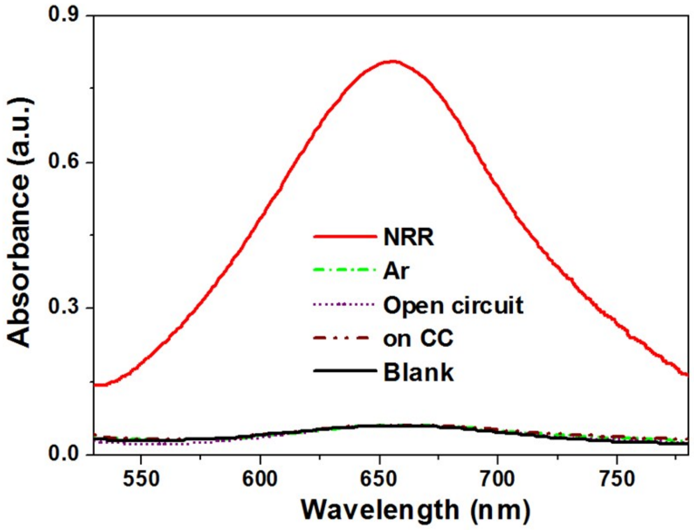

Fig. S6. UV-Vis absorption spectra of working electrolytes after 2 h of electrolysis on B-MnO_2/CC at -0.4 V in N_2-saturated solution, Ar-saturated solutions, N_2-saturated solution at open circuit, N_2-saturated solution on pristine CC and blank data.

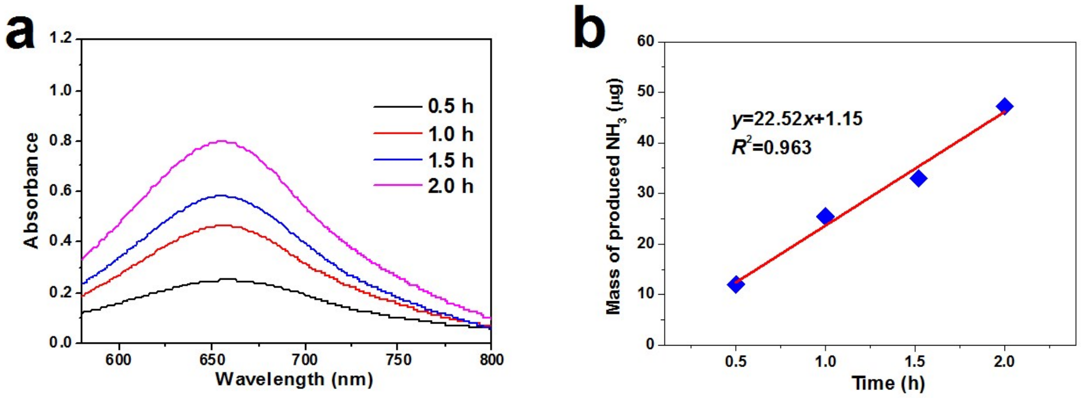

Fig. S7. (a) UV-Vis absorption spectra of the electrolytes after electrolysis at various times on B-MnO_2/CC at -0.4 V, and (b) corresponding mass of produced NH_3.

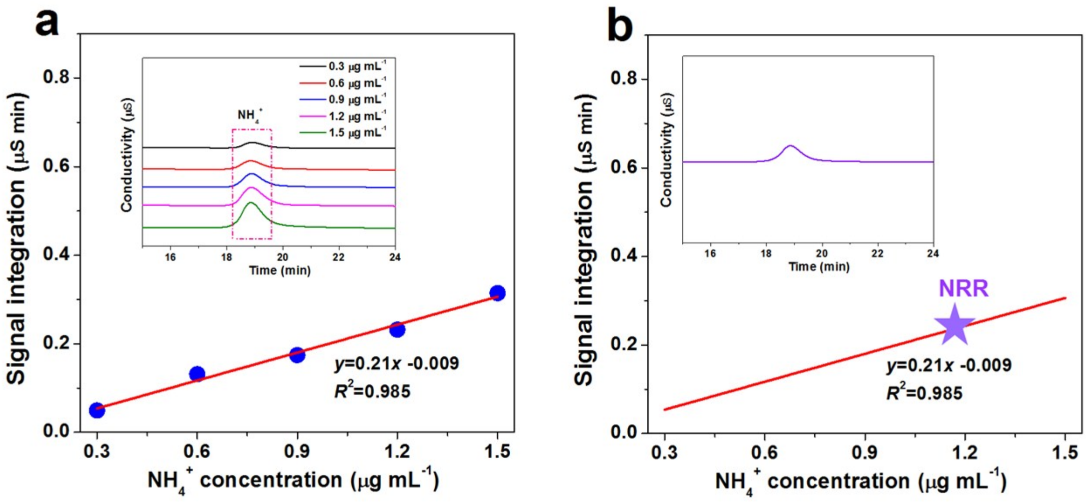

Fig. S8. (a) Ion chromatogram (IC) analysis of the NH_4^+ ions at different concentrations (inset), and corresponding calibration curve of NH_4^+ concentration vs. peak area. (b) IC spectra of the electrolyte after NRR electrolysis on B-MnO_2/CC for 2 h at -0.4 V (inset), and the determined NH_4^+ concentration of the electrolyte by referring to the calibration curve. The IC determined value is 1.15 μg mL^{-1}, consistent well with 1.23 μg mL^{-1} determined by the UV-vis analysis based on the indophenol blue method within the reasonable margin of experimental error.

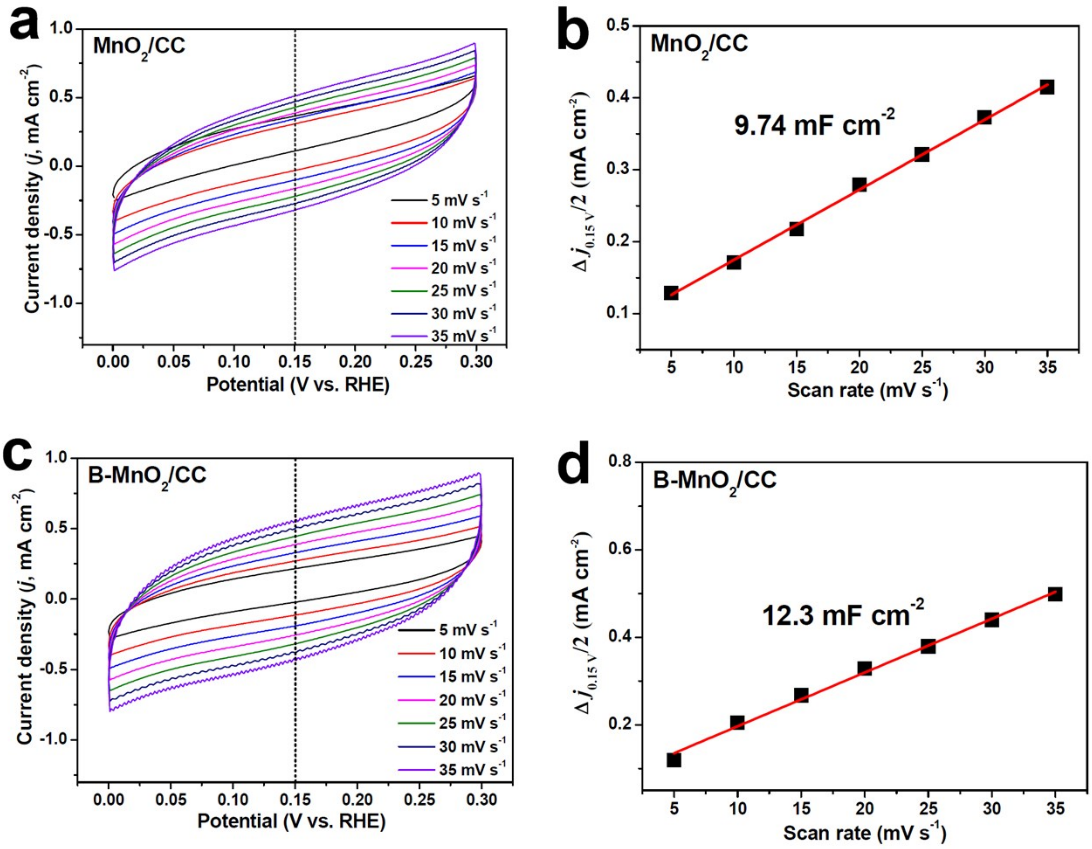

Fig. S9. Electrochemical double-layer capacitance (C_{dl}) measurements at different scanning rates of 5~35 mV s^{-1} for (a, b) MnO_2/CC and (c, d) B-MnO_2/CC.

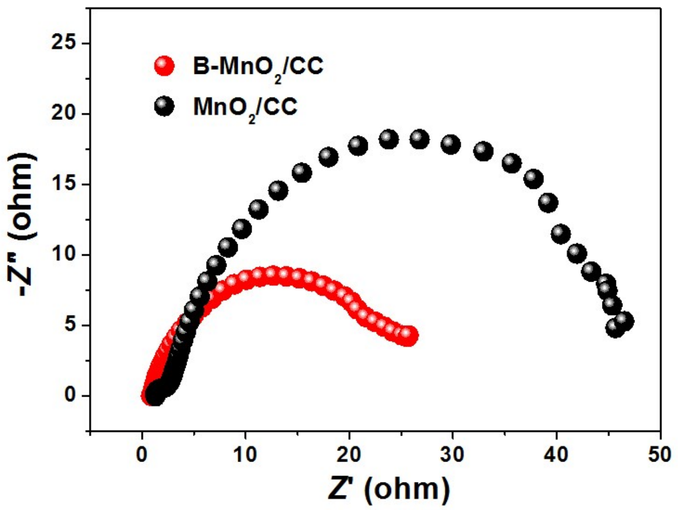

Fig. S10. Electrochemical impendence spectra of MnO_2/CC and B-MnO_2/CC.

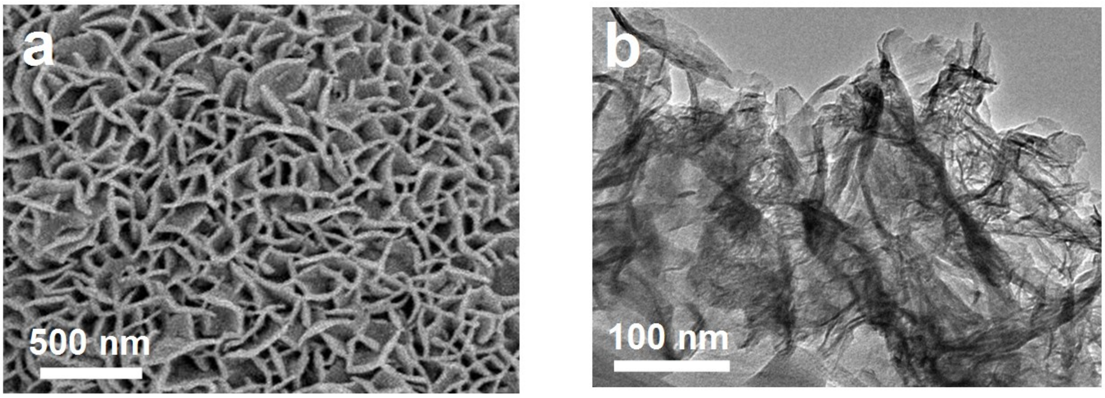

Fig. S11. Morphology of B-MnO_2/CC after stability test. (a) SEM. (b) TEM.

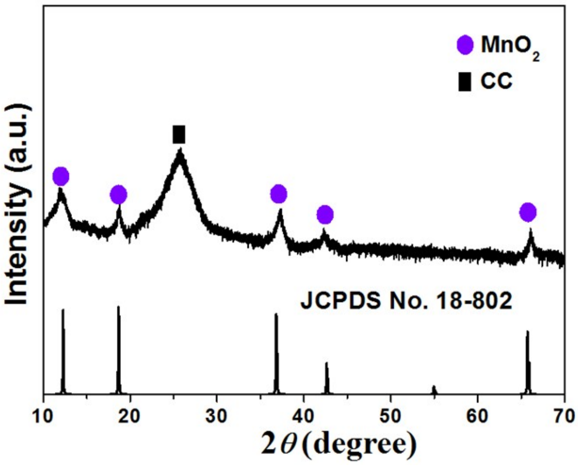

Fig. S12. XRD pattern of B-MnO$_2$/CC after stability test.

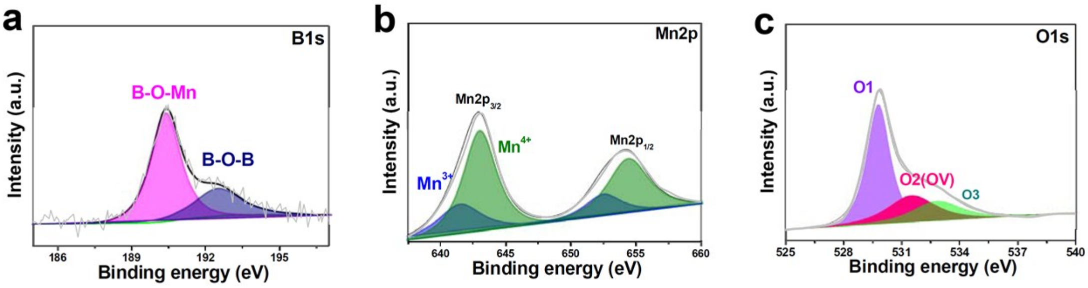

Fig. S13. XPS spectra of B-MnO_2 nanosheets scraped down from CC after stability test: (a) B1s; (b) Mn2p; (c) O1s.

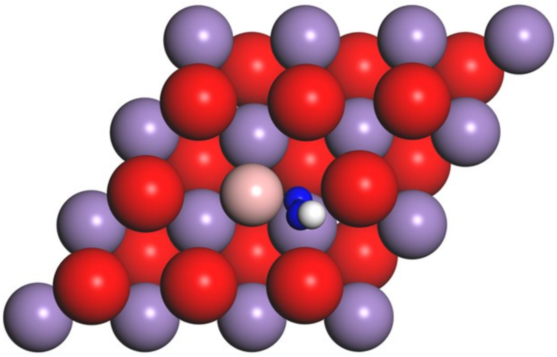

$\triangle G_{*N2H} = 1.27$ eV

$\triangle G_{*N2\text{-}*N2H} = 1.12$ eV

Fig. S14. Optimized structures of N_2H adsorption on B_O-MnO_2, and corresponding Gibbs free energies for $*N_2H$ formation (G_{*N2H}) and energy barriers for the conversion of $*N_2$ to $*N_2H$ ($\Delta G_{*N2\text{-}*N2H}$).

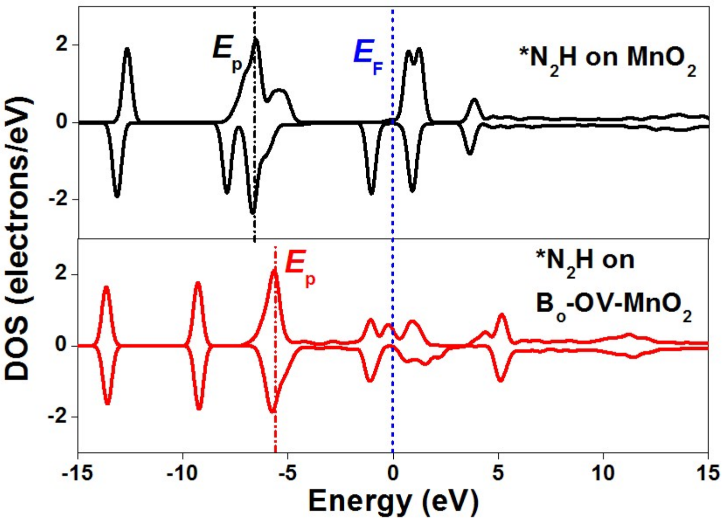

Fig. S15. PDOS of the *N_2H intermediate on MnO_2 and B_O-OV-MnO_2.

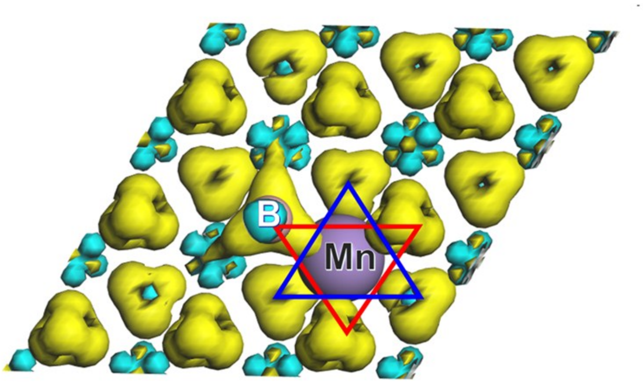

Fig. S16. Charge density distribution on B_O-MnO_2. Yellow and cyan regions correspond to the electron accumulation and depletion, respectively.

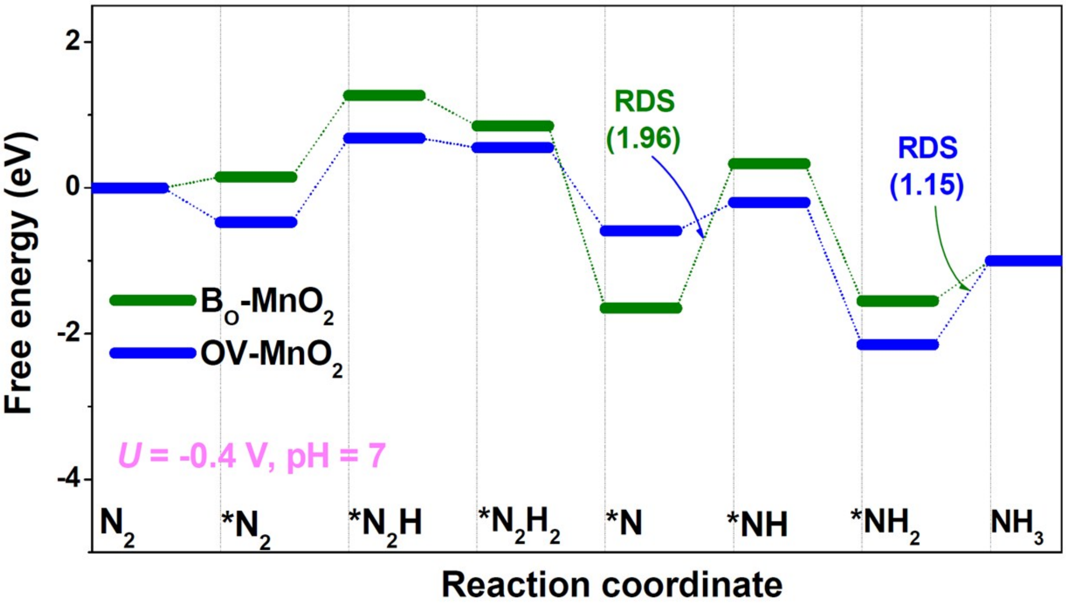

Fig. S17. Free energy diagrams of distal NRR pathway on B_O-MnO_2 and OV-MnO_2 at *U* = -0.4 V and pH = 7.

Table S1. Comparison of optimum NH_3 yield and Faradic efficiency (FE) for recently reported state-of-the-art NRR electrocatalysts at ambient conditions

Catalyst	Electrolyte	Determination method	Optimum Potential (V vs RHE)	NH_3 yield rate ($\mu g\ h^{-1}\ mg^{-1}$)	FE (%)	Ref.
Mo single atoms	0.1 M KOH	Indophenol blue method (NMR)	-0.3	34	14.6	[4]
Mosaic Bi nanosheets	0.1 M Na_2SO_4	Indophenol blue method	-0.8	13.23	10.46	[5]
Sulfur dots-graphene nanohybrid	0.5 M $LiClO_4$	Indophenol blue method	-0.85	28.56	7.07	[6]
Fe−N/C hybrid	0.1 M KOH	Indophenol blue method	-0.2	34.83	9.28	[7]
MoO_2 with oxygen vacancies	0.1 M HCl	Indophenol blue method	-0.15	12.2	8.2	[8]
CoP hollow nanocage	1.0 M KOH	Indophenol blue method	-0.4	10.78	7.36	[9]
Black phosphorus	0.01 M HCl	Indophenol blue method	-0.7	31.37	5.07 (-0.6)	[10]
Rh nanosheets	0.1 m KOH	Phenolhypochlo-rite method	-0.2	23.88	0.217	[11]
Au/CeO_x-RGO	0.1 M KOH	Salicylate method	−0.2	8.31	10.1	[12]
Au-TiO_2 sub-nanocluster	0.1 M HCl	Indophenol blue method	-0.2	21.4	8.11	[13]
Pd/C	0.1 M PBS	Indophenol blue method	0.1	4.5	8.2	[14]
Mo_2C/C	0.5 M Li_2SO_4	Nessler's reagent method	-0.3	11.3	7.8	[15]
$Ti_3C_2T_x$	0.1 M HCl	Indophenol blue method	-0.4	20.4	9.3	[16]
MoS_2 with Li-S Interactions	0.1 M Li_2SO_4	Indophenol blue method	-0.2	43.4	9.81	[17]
Fe_2O_3 nanorod	0.1 M Na_2SO_4	Indophenol blue method	-0.8	15.9	0.94	[18]
Defect-rich MoS_2 nanoflower	0.1 M Na_2SO_4	Indophenol blue method	-0.4	29.28	8.34	[19]
Nb_2O_5 nanofibers	0.1 M HCl	Indophenol blue method	-0.55	43.6	9.26	[20]
S-doped carbon	0.1 M	Indophenol blue	-0.7	19.07	7.47	[21]

nanospheres	Na_2SO_4	method				
C-doped TiO_2 nanoparticles	0.1 M Na_2SO_4	Indophenol blue method	-0.7	16.22	1.84	[22]
F-doped β-FeOOH nanorod	0.5 M $LiClO_4$	Indophenol blue method	-0.6	42.38	9.02	[23]
Defect-rich fluorographene nanosheet	0.1 M Na_2SO_4	Indophenol blue method	-0.7	9.3	4.2	[24]
MoO_3 nanosheets	0.1 M HCl	Indophenol blue method	-0.5	29.43	1.9	[25]
MoO_2/graphene	0.1 M Na_2SO_4	Indophenol blue method	-0.35	37.4	6.6	[26]
Cr_2O_3/RGO	0.1 M HCl	Indophenol blue method	-0.6	33.3	7.33	[27]
MnO particles	0.1 M Na_2SO_4	Indophenol blue method	-0.39	7.92	8.02	[28]
Mn_3O_4 nanocubes	0.1 M Na_2SO_4	Indophenol blue method	-0.8	11.6	3	[29]
Mn_3O_4/RGO	0.1 M Na_2SO_4	Indophenol blue method	-0.85	17.4	3.52	[30]
MnO_2–$Ti_3C_2T_x$ MXene nanohybrid	0.1 M HCl	Indophenol blue method	-0.55	34.12	11.39	[31]
B-MnO_2/CC	0.5 M $LiClO_4$	Indophenol blue method	-0.4	54.2	16.8 (-0.2V)	This work

Supplementary references

[1]. D. Zhu, L. Zhang, R. E. Ruther and R. J. Hamers, *Nat. Mater.*, 2013, **12**, 836.

[2]. G. W. Watt and J. D. Chrisp, *Anal. Chem.*, 1952, **24**, 2006-2008.

[3]. S. J. Clark, M. D. Segall, C. J. Pickard, P. J. Hasnip, M. I. J. Probert, K. Refson and M. C. Payne, *Z. Kristallogr.*, 2005, **220**, 567-570.

[4]. L. Han, X. Liu, J. Chen, R. Lin, H. Liu, F. Lu, S. Bak, Z. Liang, S. Zhao and E. Stavitski, *Angew. Chem. Int. Edit.*, 2018, **58**, 2321-2325.

[5]. L. Li, C. Tang, B. Xia, H. Jin, Y. Zheng and S.-Z. Qiao, *ACS Catal.*, 2019, **9**, 2902-2908.

[6]. H. Chen, X. Zhu, H. Huang, H. Wang, T. Wang, R. Zhao, H. Zheng, A. M. Asiri, Y. Luo and X. Sun, *Chem. Commun.*, 2019, **55**, 3152-3155.

[7]. Y. Wang, X. Cui, J. Zhao, G. Jia, L. Gu, Q. Zhang, L. Meng, Z. Shi, L. Zheng and C. Wang, *ACS Catal.*, 2018, **9**, 336-344.

[8]. G. Zhang, Q. Ji, K. Zhang, Y. Chen, Z. Li, H. Liu, J. Li and J. Qu, *Nano Energy*, 2019, **59**, 10-16.

[9]. W. Guo, Z. Liang, J. Zhao, B. Zhu, K. Cai, R. Zou and Q. Xu, *Small Methods*, 2018, **2**, 1800204.

[10]. L. L. Zhang, L. X. Ding, G. F. Chen, X. F. Yang and H. H. Wang, *Angew. Chem. Int. Edit.*, 2019, **131**, 2638-2642.

[11]. H. M. Liu, S. H. Han, Y. Zhao, Y. Y. Zhu, X. L. Tian, J. H. Zeng, J. X. Jiang, B. Y. Xia and Y.

Chen, *J. Mater. Chem. A*, 2018, **6**, 3211-3217.

[12]. S. J. Li, D. Bao, M. M. Shi, B. R. Wulan, J. M. Yan and Q. Jiang, *Adv. Mater.*, 2017, **29**, 1700001.

[13]. M. M. Shi, D. Bao, B. R. Wulan, Y. H. Li, Y. F. Zhang, J. M. Yan and Q. Jiang, *Adv. Mater.*, 2017, **29**, 1606550.

[14]. J. Wang, L. Yu, L. Hu, G. Chen, H. Xin and X. Feng, *Nat. Commun.*, 2018, **9**, 1795.

[15]. H. Cheng, L. X. Ding, G. F. Chen, L. Zhang, J. Xue and H. Wang, *Adv. Mater.*, 2018, **30**, 1803694.

[16]. J. Zhao, L. Zhang, X.-Y. Xie, X. Li, Y. Ma, Q. Liu, W.-h. Fang, X. Shi, G. Cui and X. Sun, *J. Mater. Chem. A*, 2018, **6**, 24031-24035.

[17]. Y. Liu, M. Han, Q. Xiong, S. Zhang, C. Zhao, W. Gong, G. Wang, H. Zhang and H. Zhao, *Adv. Energy. Mater.*, 2019, **9**, 1803935.

[18]. X. Xiang, Z. Wang, X. Shi, M. Fan and X. Sun, *Chemcatchem*, 2018, **10**, 4530-4535.

[19]. X. Li, T. Li, Y. Ma, Q. Wei, W. Qiu, H. Guo, X. Shi, P. Zhang, A. M. Asiri and L. Chen, *Adv. Energy. Mater.*, 2018, **8**, 1801357.

[20]. J. Han, Z. Liu, Y. Ma, G. Cui, F. Xie, F. Wang, Y. Wu, S. Gao, Y. Xu and X. Sun, *Nano Energy*, 2018, **52**, 264-270.

[21]. L. Xia, X. Wu, Y. Wang, Z. Niu, Q. Liu, T. Li, X. Shi, A. M. Asiri and X. Sun, *Small Methods*, 2018, **3**, 1800251.

[22]. Y. Wang, Q. Pan, B. Zhong, Y. Luo, G. Cui, X.-D. Guo and X. Sun, *Nanoscale Adv.*, 2019, **1**, 961-964.

[23]. X. Zhu, Z. Liu, H. Wang, R. Zhao, H. Chen, T. Wang, F. Wang, Y. Luo, Y. Wu and X. Sun, *Chem. Commun.*, 2019, **55**, 3987-3990.

[24]. J. Zhao, J. Yang, L. Ji, H. Wang, H. Chen, Z. Niu, Q. Liu, T. Li, G. Cui and X. Sun, *Chem. Commun.*, 2019, **55**, 4266-4269.

[25]. J. Han, X. Ji, X. Ren, G. Cui, L. Li, F. Xie, H. Wang, B. Li and X. Sun, *J. Mater. Chem. A*, 2018, **6**, 12974-12977.

[26]. J. Wang, Y. P. Liu, H. Zhang, D. J. Huang and K. Chu, *Catal. Sci. Technol.*, 2019, **9**, 4248-4254.

[27]. L. Xia, B. Li, Y. Zhang, R. Zhang, L. Ji, H. Chen, G. Cui, H. Zheng, X. Sun, F. Xie and Q. Liu, *Inorg. Chem.*, 2019, **58**, 2257-2260.

[28]. Z. Wang, F. Gong, L. Zhang, R. Wang, L. Ji, Q. Liu, Y. Luo, H. Guo, Y. Li, P. Gao, X. Shi, B. Li, B. Tang and X. Sun, *Adv. Sci.*, 2018, 1801182.

[29]. X. Wu, L. Xia, Y. Wang, W. Lu, Q. Liu, X. Shi and X. Sun, *Small*, 2018, **14**, 1803111.

[30]. H. Huang, F. Gong, Y. Wang, H. Wang, X. Wu, W. Lu, R. Zhao, H. Chen, X. Shi, A. M. Asiri, T. Li, Q. Liu and X. Sun, *Nano Res.*, 2019, **12**, 1093-1098.

[31]. W. Kong, F. Gong, Q. Zhou, G. Yu, L. Ji, X. Sun, A. M. Asiri, T. Wang, Y. Luo and Y. Xu, *J. Mater. Chem. A*, 2019, **7**, 18823-18827.